photonics

MDPI

Article

Demonstration of Quantum Polarized Microscopy Using an Entangled-Photon Source

Mousume Samad [1,2,*], Maki Shimizu [1] and Yasuto Hijikata [1,*]

[1] Department of Electrical and Electronic Systems Engineering, Faculty of Engineering, Saitama University, 255 Shimo-Okubo, Saitama-shi, Saitama 338-8570, Japan; maki2@mail.saitama-u.ac.jp
[2] Department of Information and Communication Engineering, Bangladesh Army University of Engineering and Technology (BAUET), Qadirabad 6431, Bangladesh
* Correspondence: samad.m.128@ms.saitama-u.ac.jp (M.S.); yasuto@mail.saitama-u.ac.jp (Y.H.)

Abstract: With the advancement of non-classical light sources such as single-photon and entangled-photon sources, innovative microscopy based on quantum principles has been proposed for traditional microscopy. This paper introduces the experimental demonstration of a quantum polarization microscopic technique that incorporates a quantum-entangled photon source. Although the point that employs the variation in polarization angle due to reflection or transmission at the sample is similar to classical polarization microscopy, the method for constructing the image contrast is significantly different. The image contrast is constructed by the coincidence count of signal and idler photons. In the case that the coincidence count is recorded from both the signal and idler photons, the photon statistics resemble a thermal state, similar to the blackbody radiation, but with a significantly higher peak intensity in the second-order autocorrelation function at zero delay that is derived from the coincidence count, while, when the coincidence count is taken from either the signal or idler photon only, although the photon state exhibits a thermal state again, the photon statistics become more dispersive and result in a lower peak intensity of the autocorrelation function. These different thermal states can be switched by slightly changing the photon polarization, which is suddenly aroused within a narrow range of the analyzer angle. The autocorrelation function $g^2(0)$ at the thermal state exhibits a sensitivity that is three times higher compared to the classical coincidence count rate, and this concept can be effectively utilized to enhance the contrast of the image. One of the key achievements of our proposed method is ensuring a low power of illumination (in the order of Pico-joules) for constructing the image. In addition, the robustness without any precise setup is also favorable for practical use. This polarization microscopic technique can provide a superior imaging technique compared to the classical method, opening a new frontier for research in material sciences, biology, and other fields requiring high-resolution imaging.

Keywords: quantum imaging; quantum-entangled photon source; thermal state; black body radiation; classical optical microscopy

Received: 8 January 2025
Revised: 27 January 2025
Accepted: 29 January 2025
Published: 31 January 2025

Citation: Samad, M.; Shimizu, M.; Hijikata, Y. Demonstration of Quantum Polarized Microscopy Using an Entangled-Photon Source. *Photonics* **2025**, *12*, 127. https://doi.org/10.3390/photonics12020127

1. Introduction

Optical microscopy and spectroscopy play significant roles in modern research across a wide range of disciplines, including fundamental physics, materials science, chemical studies, and biological sciences. In optical microscopy, it is fascinating to observe how historical advancements in light properties have consistently led to the creation of innovative imaging applications. Optical imaging with classical light is limited in terms of the

signal-to-noise ratio, resolution, contrast, and spectral range [1]. To overcome these limitations, quantum properties of light utilizing correlated, entangled, or squeezed photons have been innovated for optical imaging [2–6]. In addition to this, quantum imaging might serve the extremely robust and highly resistive measurements against various kinds of perturbations such as mechanical vibration, the fluctuation of surrounding circumstances or the light source, and so on. The initial demonstration of entangled-photon sources, known as the bi-photon state, has led to numerous applications in quantum imaging [7–9]. In particular, the essential features of entangled-photon sources are the polarization state, momentum, energy, and position correlations of the entangled-photon pair [10,11]. The entangled-photon source can enable the imaging technique in spectral ranges where efficient detection is challenging, or even imaging with light that does not directly interact with the sample [12–15]. Moreover, utilizing specific quantum states of light and their photon statistics allows for sensing and imaging beyond the constraints of classical techniques. The quantum optical microscopy with an entangled-photon source can construct an image with extremely low light intensity when applying quantum light, enabling new insights into photosensitive biochemical applications. At present, polarization-entangled-photon sources have been a key for these works of research due to their simplicities in generation, control, and measurement. The entangled-photon pairs from these sources can be produced through spontaneous parametric down-conversion (SPDC) [16]. In classical imaging methods, the key technology is extracting the phase information by interfering with a reference beam. It is impossible to extract phase information from classical interference measurements when incoherent and unpolarized beams are used, whereas the coherence of the polarization-entangled state allows for the extraction of images despite dynamic phase disorder and significant classical noise [5]. In optical microscopy, there are some challenges for biological measurement such as the need to increase the power to improve the resolution while also decreasing the power to prevent photo damage to the biological structure. This creates a trade-off between the resolution and photo damage. Moreover, the low illumination power leads to a reduction in the resistivity against noise. In contrast, quantum polarization microscopy with an entangled-photon source can be carried out at an extremely low light intensity to enable new insights into photosensitive biomedical applications.

Ref. [17] demonstrates an optical microscopy technique capable of optical phase measurement beyond the standard quantum limit (SQL). In this case, improving the signal-to-noise ratio (SNR) is crucial, and entanglement plays a fundamental role in achieving this enhancement [18,19]. However, one limitation of their approach is that it requires optical path length accuracies on the order of several tens of micrometers [17]. Additionally, quantum imaging utilizing spatial and polarization entanglement for biological organisms is described in Ref. [20]. This approach, known as imaging by coincidence from entanglement (ICE), provides a high SNR, a greater resolvable pixel count, and a full birefringence-quantified quantum imaging technique that produces high-quality images of biological samples. Quantum microscopy at the Heisenberg limit, proposed in Ref. [21], involves coincidence quantum microscopy (QMC) with balanced path lengths, enabling super-resolution imaging with substantially higher speeds and contrast-to-noise ratios (CNRs) compared to existing wide-field quantum imaging methods. Despite these advantages, these techniques are significantly affected by a low SPDC efficiency or detector limits. For example, in the case of quantum holography using polarization entanglement [5], it requires tens of hours for image acquisition due to the low frame rate of EMCCD cameras. In contrast, our proposed method achieves image acquisition in much less time.

In this paper, to overcome the issues above, we propose an imaging technique involving measurements of coincidence counts and the autocorrelation function at zero

delay, $g^2(0)$, using a quantum polarized type II entangled-photon source. According to our method, the variation in polarization angle due to reflection or transmission at the sample is detected using two distinct thermal states of SPDC photon statistics. Namely, since it switches between the two different states depending on whether either the signal or idler port is in a vacuum state or not, by setting the analyzer at the sample side to block the photon, the image contrast is constructed due to the transition between the states. It should be also noticed that our method offers a significant advantage in that it does not require precise optical setups, such as beam alignment, path difference adjustments (delay lines), or phase drift cancellation, which are commonly needed in quantum phase-sensing measurements. Instead, we employ polarization-sensing measurements to provide a more convenient and robust measurement technique. By adopting this approach, we aim to develop a high-performance and reliable imaging technique with a simple setup based on polarization sensing.

2. Methods

The entangled-photon-pair source used in this experiment exhibits bunching characteristics, a phenomenon associated with the photon statistical properties of light. This behavior, where photons arrive in pairs or "bunches" rather than independently, is typical in SPDC and confirms the photon-pair generation. Actually, the bunching effect is observed in the second-order autocorrelation measurement, $g^2(\tau)$, between signal and idler photons [22]. In general, thermal state exhibits bunching characteristic, as shown by the autocorrelation at zero delay larger than 1 ($g^2(0) > 1$.) However, different from the case of ordinary thermal state like black-body radiation, a higher bunching peak is seen in the case of SPDC photon statistics because the time interval between photon pairs [Signal and Idler] is longer compared to the Poisson case ($g^2(0) = 1$) or super-Poisson ($g^2(0) > 1$) [23], leading to the enhancement in photon-bunching. Here, this photon state is called 'hyper-Poisson state.' Figure 1a shows the schematic illustration of the variations of $g^2(\tau)$ with respect to the time delay (τ) in the cases of hyper-Poisson and super-Poisson states. On the other hand, when either the signal or the idler photon is blocked using an analyzer (or polarizer), a bunching peak with lower intensity is seen as the super-Poisson state. This is due to the fact that the time interval tends to cluster together more than in a Poisson distribution [23] and the photon number for each photon pulse becomes more dispersive than in the case of a hyper-Poisson state. This will be experimentally confirmed in Figure 2. It is noticed that the coincidence window for measurements should be sufficiently smaller than the width of the bunching peak ($\Delta\tau$) to observe the bunching peak correctly. The transition between the hyper-Poisson and super-Poisson state occurs when either the signal or idler photons are blocked/transmitted by the analyzer introduced into the beam path. This transition happens rapidly and smoothly, even with minimal perturbation, resulting in a sharp dip in the $g^2(0)$ curve, as shown in Figure 1b.

In this research, optical imaging is constructed through the coincidence count rate or the autocorrelation function at zero delay $g^2(0)$ between signal and idler photon with respect to the polarizer angle. These functions are schematically illustrated in Figure 1b. The coincidence count rate mostly follows a sinusoidal curve, as does the transmitted light intensity when the polarizer is rotated. When the coincidence rate approaches zero, which induces the switching from the hyper-Poisson state to the super-Poisson state, the $g^2(0)$ curves indicates a sharp dip as shown in the figure. Therefore, these count rate variations can be used for constructing an image. Conversely, in the polarizer angle range where these count rates are almost constant such as the flat regions in $g^2(0)$ or the coincidence rate at minimum or maximum points, contrast is hardly obtained. Since the sharpness of this

dip correlates directly with the image contrast, the autocorrelation imaging may have the capability to provide a higher contrast than that of a coincidence rate.

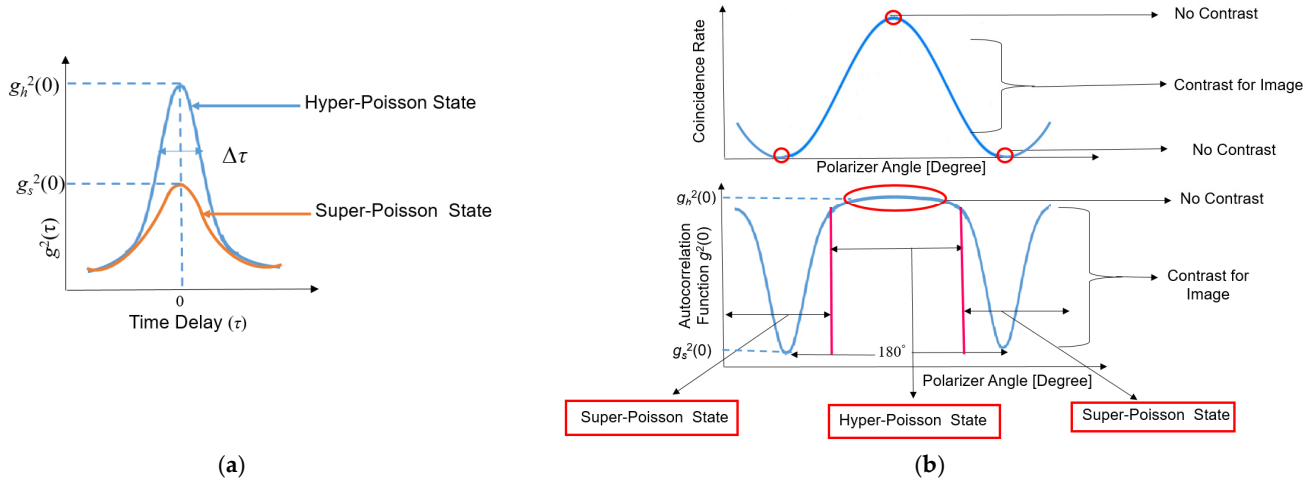

Figure 1. Concept of the imaging methodology: (**a**) second-order autocorrelation function $g^2(\tau)$ for hyper-Poisson and super-Poisson states; and (**b**) coincidence rate and autocorrelation function at zero delay $g^2(0)$ as a function of polarization angle.

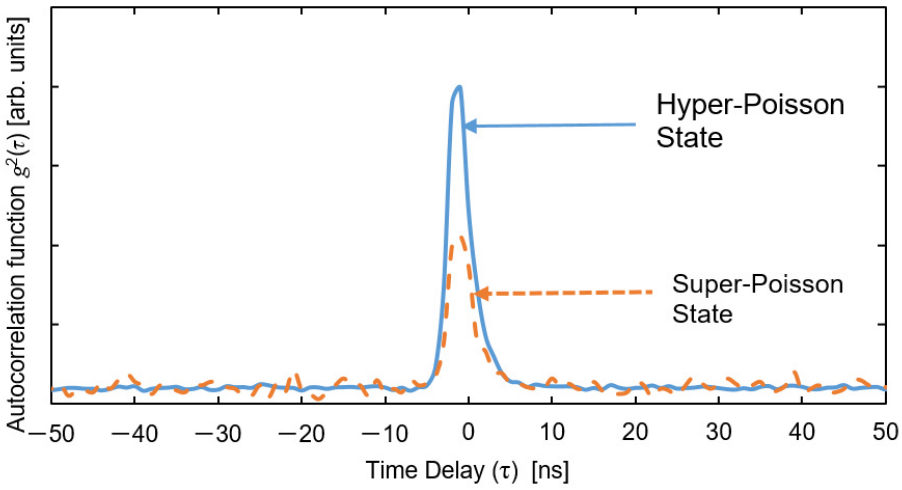

Figure 2. Experimental results of $g^2(\tau)$ versus time delay (τ) between signal and idler port for hyper-Poisson state and super-Poisson state.

As mentioned above, since the coincidence rate varies almost sinusoidal with respect to the polarization angle, the width of peak (dip) in the curve is $\pi/4$ radians, which corresponds to the dynamic range of the measurement, while the width of the autocorrelation function is attributed to fluctuations in the SPDC process. In an entangled-photon source based on SPDC, the time interval of the entangled-photon pair varies slightly due to inherent statistical fluctuations in the emission process. These fluctuations result in a spread in the photon's arrival times at the detectors which corresponds to the width of the dips in $g^2(0)$ plots.

In the present work, the schematic arrangement of quantum polarized microscopy is depicted in Figure 3. The correlated photon-pair source with a collinear type II spontaneous parametric down-conversion (SPDC), operating wavelength (810 ± 2 nm), and maximum photon pairs per second (>450 kHz) were used as the entangled-photon source. In this system, the signal photons are vertically polarized, while the idler photons are horizontally polarized, and both are transmitted through polarization-maintaining single-mode fibers. Two analyzers are positioned in front of the photon-counting detector—one remains

fixed, while the other can be rotated—followed by a band-pass filter (810 ± 5 nm) used to minimize stray light. The signal and idler photons were detected using avalanche photodiode (APD) detectors connected via multimode optical fibers. The photon counting of each detector, and coincidence counts and delay adjustment between two detectors, were performed by a time correlator.

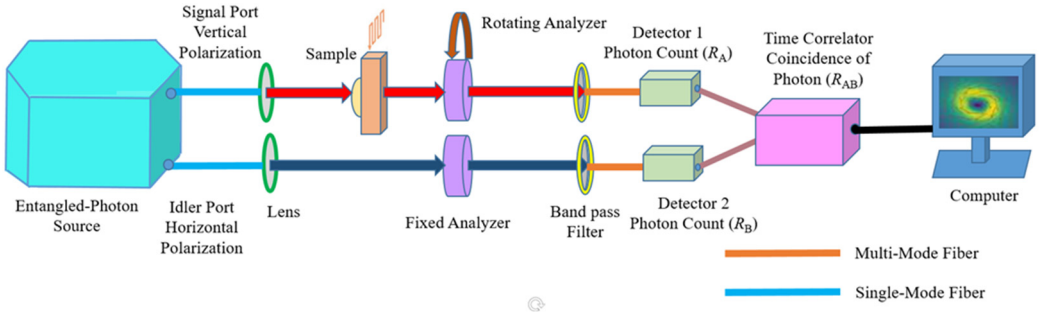

Figure 3. Schematic view of the imaging system.

To demonstrate the proposed imaging method, a first-order (m = 1) optical spiral retarder sample has been used in this experiment. This sample converts a linearly polarized source into radially or azimuthally polarization. Figure 4 illustrates the phenomenon where a linearly polarized beam is incident on the first-order optical spiral retarder. When a linear polarization beam is incident (Figure 4a), since the fast axis orientation of the sample is designed to rotate by half-angle of azimuth angle, as shown in Figure 4b, the output polarization is aligned radially (Figure 4c).

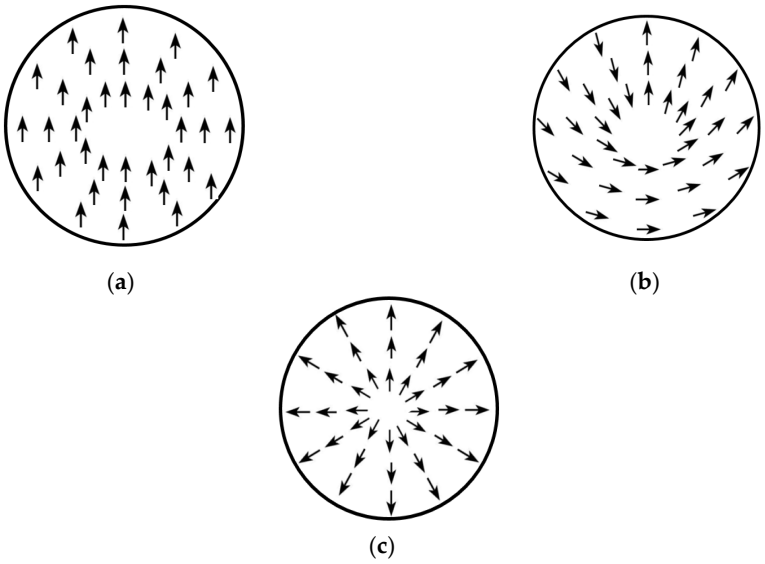

Figure 4. Schematic illustrations for the optical spiral retarder: (**a**) linearly polarized input beam incident on optical spiral retarder; (**b**) fast axis orientation of optical spiral retarder; and (**c**) output polarization after a linearly polarized beam passed through the optical spiral retarder.

The sample is scanned using a motorized stage and photon counting for each point is recorded via the time correlator. By analyzing the experimental data, including the coincidence count and autocorrelation function $g^2(0)$, the final images are constructed.

3. Results

First of all, to obtain proper coincidence windows (Δt) under the hyper-Poisson state and super-Poisson state, we measured the autocorrelation function $g^2(\tau)$ as a function of

the time delay (τ) between channel A and B with the analyzer angles at 110° (hyper-Poisson state) and 20° (super-Poisson state). Figure 2 shows the experimental results of $g^2(\tau)$ for both cases of the hyper-Poisson state and the super-Poisson state. The hyper-Poisson state exhibits a significantly higher bunching peak compared to the super-Poisson state as mentioned above. In addition, it was found that a coincidence window of 15 ns is sufficient for simultaneously counting signal and idler photons for both the hyper-Poisson state and super-Poisson state.

The autocorrelation function at the zero-delay, $g^2(0)$, can be determined using the following equation [24]:

$$g^2(0) = \frac{R_{AB}(0)}{R_A \cdot R_B \cdot \Delta t} \tag{1}$$

where R_A, R_B, and R_{AB} are the count rate of the beam pass with the rotating analyser (channel A) and that of the fixed analyser (channel B), and coincidence count rate of channel A and B, respectively. Figure 5 shows the coincidence count and the autocorrelation function $g^2(0)$ versus the analyzer angle for different integration times, including 10, 20, 40, and 80 s. All the coincidence count rate exhibits a sinusoidal curve with respect to the analyzer angle, similar to the classical polarization measurement. However, unlike normal optical interference measurements, it should be noted that the interference-like pattern is obtained from the coincidence of photons on the two different paths, rather than the two paths of light waves interfering with each other. On the other hand, the plot of the autocorrelation function concerning the analyzer angle distinguishes between the super-Poisson state, which features a sharp dip region, and the hyper-Poisson state, characterized by a flat region. From these results, it is expected that the proposed method enables us to realize an imaging technique with high robustness and high stability because it requires no real light-wave interference but only the time-correlation of electrical pulse signal.

Here, we assume that the sharp dips in the super-Poisson state can be described using the Gaussian distribution function. The measurement of time-correlation experiments typically follows a Gaussian distribution due to the statistical nature of random fluctuations, arbitrariness, and timing uncertainties, which contribute to the spread of the measured experimental values.

In this case, the dip expressed with the following equation was obtained through a curve-fitting analysis of the experimental data:

$$\mathrm{y} = \mathrm{y}_0 + \mathrm{A}\exp\left[-4\ln 2 \times \left\{\frac{(x - x_c)}{\mathrm{FWHM}}\right\}^2\right] \tag{2}$$

The red solid lines in the $g^2(0)$ plots in Figure 5 show the fitted curves using Equation (2). Note that curve fitting has been performed twice for each integration time because there are two dips in the analyzer angle range measured ($0-220°$). The standard deviations obtained from the curve fits to the measured data are shown in Table 1.

As the integration time increases, the error is progressively reduced, leading to an improvement in the SNR. Meanwhile, the increase in integration time leads to an increase in total measurement time. It is suggested that the integration time of 20 s is enough to obtain a moderate image contrast.

The coincidence rate exhibits a sinusoidal curve, similar to the methodology used in classical polarization microscopy. Therefore, the contrast of a coincidence rate image can be regarded as similar to a classical image. However, it is suggested that the coincidence rate image can be obtained by an extremely low-power illumination. Additionally, the image contrast might be further enhanced using the autocorrelation function compared to the coincidence rate image, owing to the abrupt change in the polarization angle dependence.

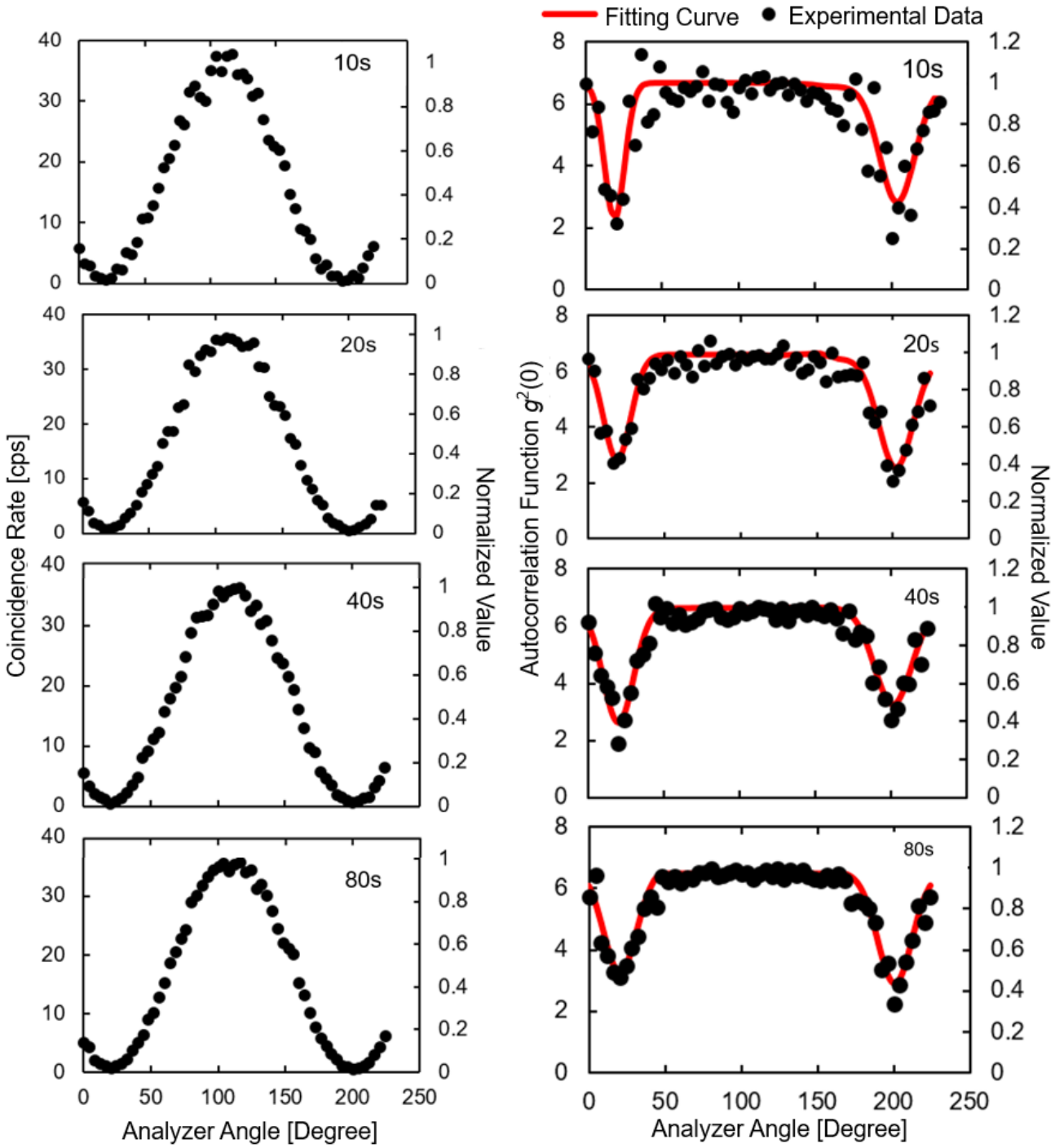

Figure 5. Coincidence count and autocorrelation function at zero delay $g^2(0)$ versus analyzer angle at different integration times.

Table 1. Standard deviation, maximum sensitivity, and dynamic range obtained from curve fits for the autocorrelation function at different integration times.

Integration Time	Standard Deviation (%)		Maximum Sensitivity [/°]		Dynamic Range [°]	
	1st Dip	2nd Dip	1st Dip	2nd Dip	1st Dip	2nd Dip
10 s	9.1	11	0.057	0.028	15.4	27
20 s	5.4	7.1	0.037	0.031	21.1	26.4
40 s	5.1	5.5	0.035	0.024	23.6	28.9
80 s	5.8	5.2	0.027	0.028	25.6	26.5

Here, we defined that the maximum sensitivity and dynamic range correspond to the maximum gradient and the full width at half maximum (FWHM), respectively. For the coincidence rate, the maximum sensitivity and dynamic range are found to be $\pi/180$ [/°] and 90 [°], respectively. The maximum sensitivities and dynamic ranges obtained from curve fitting for the autocorrelation function are presented in Table 1. As shown in the table, the maximum sensitivity for the autocorrelation function is several times higher than that of the coincidence rate in general, while the dynamic range is lower.

As mentioned before, the depth of the dip in the autocorrelation function corresponds to the $g^2(0)$ value in the super-Poisson state. As the thermal photon generation rate increases, the $g^2(0)$ value decreases, which makes the dip more pronounced.

To demonstrate our imaging method, a spiral retarder optical sample has been utilized. Figure 6a presents the photo of the spiral retarder optical sample with a diameter of 25.4 mm, consisting of a black part and areas of free space. The dimension of the image is 30 × 30 mm. The images are obtained using predefined experimental parameters, including the integration time (20 s) and coincidence window (15 ns). The two-dimensional (2D) scan images of the coincidence image and the autocorrelation image are displayed in Figure 6b,c, respectively. As shown in the figures, the image derived from the coincidence counts shows that the image contrast is given in a sinusoidal manner according to the azimuth angle; namely, the contrast becomes stronger in areas corresponding to nodes (coincidence count at around 70 or 160° shown in Figure 5), while it becomes weaker in areas corresponding to antinodes (coincidence count at around 25 or 115° shown in Figure 5).

For the autocorrelation function $g^2(0)$ image, the dark area, corresponding to the dip region under the super-Poisson state, reveals the strong contrast and the bright area (i.e., the flat region under the hyper-Poisson state) weak contrast. Figure 6d, e compare the contrast from the coincidence rate with the autocorrelation function $g^2(0)$ at the purple solid bars and the black solid bars, respectively, shown in Figure 6b,c. In Figure 6d, the line profile along the purple solid line exhibits a greater contrast in the autocorrelation function compared to the coincidence count. Conversely, in Figure 6e, the line profile along the black solid line shows a better contrast in the coincidence count than in the autocorrelation function. These results can be attributed to the fact that the autocorrelation function produces a sharp dip near a coincidence count of approximately zero, where the coincidence count remains relatively unchanged. In contrast, in regions where the coincidence count varies significantly, the autocorrelation function remains nearly constant. Therefore, even if the sample induces a slight polarization rotation, it is expected to obtain a high-contrast image by setting the polarization direction of the sample-transmitted light to be in the dip bottom under a super-Poisson state.

In the measurements, the optical power applied to the sample for obtaining the image was about 0.1 pJ, which is a remarkably low irradiation power compared to conventional imaging techniques. Therefore, it is suggested that our proposed method can be applicable for biological systems that are easily damaged against photo-irradiation. Furthermore, a sample in a dispersive interference medium such as wet organ tissues can be clearly observed because dispersive interference can be avoided owing to the basis of quantum interference. Obviously, these advantages can pave the way for a new frontier in biomedical imaging for biological systems.

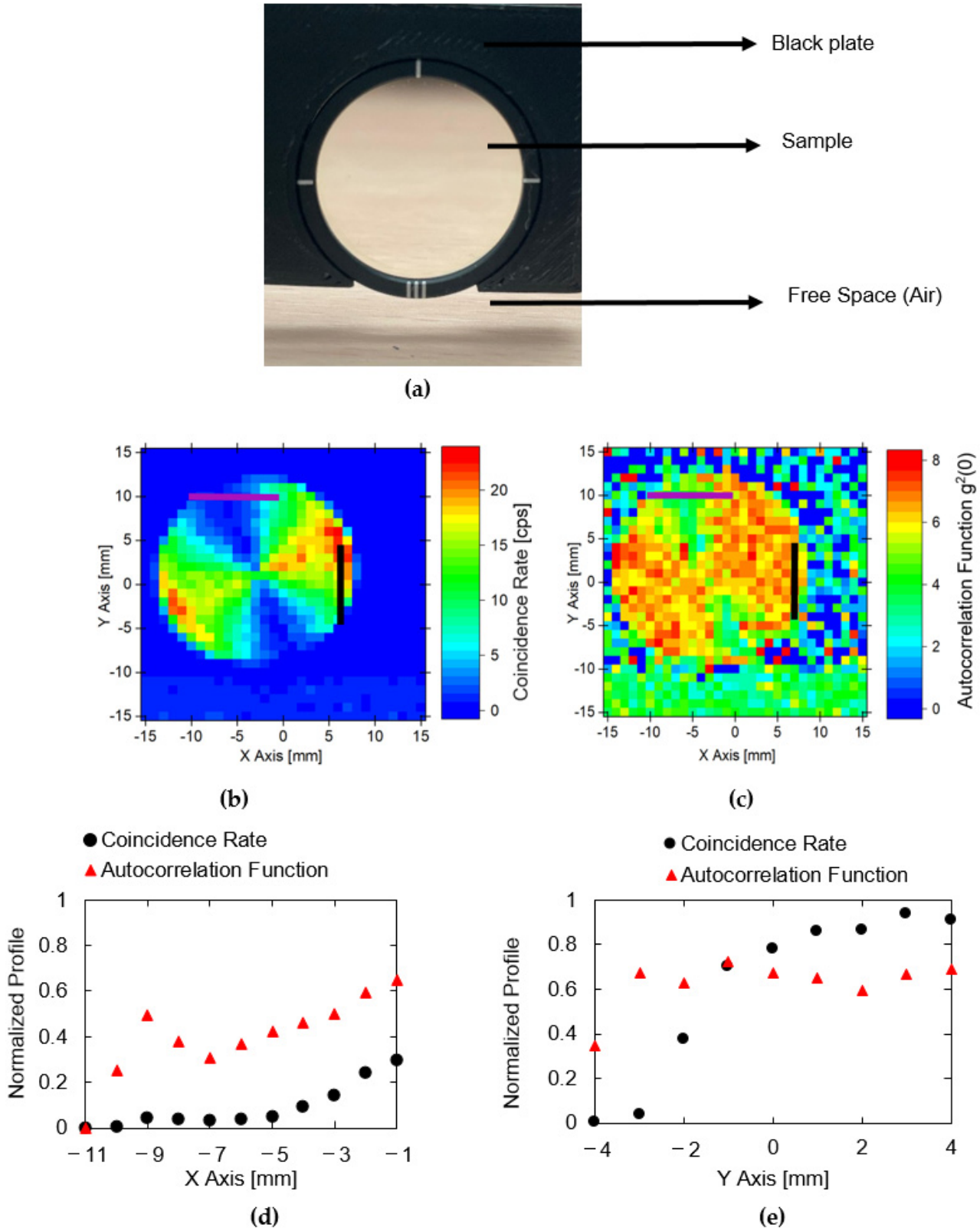

Figure 6. (**a**) Photograph of optical spiral retarder sample (diameter of sample: 25.4 mm); (**b**) coincidence image of spiral retarder; (**c**) autocorrelation Image of spiral retarder; (**d**) one-dimensional line-scanned profile highlighted in purple solid line from the coincidence rate and autocorrelation function image; and (**e**) one-dimensional line-scanned profile highlighted in black solid line from the coincidence rate and autocorrelation function image.

4. Discussion

According to Ono et al. [17], the quantum entanglement is crucial for enhancing the signal-to-noise ratio (SNR) in phase measurements beyond the standard quantum limit (SQL). In their work, the SNR achieved with quantum entanglement is 17.7 ± 1.22. Moreover, in the method proposed in Ref. [5], the SNR values range between 19 and 21.

To compare our proposed method with these existing works, the systematic analysis of the signal-to-noise ratio in bipartite is defined as the ratio of the "mean contrast" to its standard deviation (mean fluctuation) [25]. The SNR value for the proposed method can be derived using the following equation [3]:

$$\mathrm{SNR_s} = \frac{|< s_{\mathrm{in}} - s_{\mathrm{out}} >|}{\sqrt{< \delta^2 (s_{\mathrm{in}} - s_{\mathrm{out}}) >}} \tag{3}$$

where S_{in} represents the average photon count rate at the signal port section before inserting the sample, S_{out} is the average photon count rate at the signal port section after inserting the sample, and $\delta^2(S_{\mathrm{in}} - S_{\mathrm{out}})$ represents the statistical fluctuation or uncertainty in the difference between $\mathrm{S_{in}}$ and $\mathrm{S_{out}}$. Consequently, the value of the SNR for the present experiments was found to be 19.7, which is comparable to the SNR value reported in the Ref. [5] and Ref. [17].

5. Conclusions

In summary, we proposed a new polarization microscopic method, in which the switching super-Poisson state and hyper-Poisson state of entangled photons by the polarization angle variation can significantly enhance the image contrast in microscopy. Our method was demonstrated through the observation of an optical spiral retarder sample. We revealed that this imaging technique is enabled by a quantum-source, which does not rely on classical optical coherence, offering substantial improvements over classical polarization imaging techniques in terms of robustness and stability. Furthermore, this approach mitigates the susceptibility to photo-damage and photo-bleaching often associated with high-intensity laser beams. This technological breakthrough promises to expand new horizons in exploring the mechanical properties of live biological systems. However, the fluctuation noise is suggested as the current issue of our imaging technique, resulting in the increase in measurement time. In addition, although the entangled-photon beam was not focused at present, it should be focused with the lens to improve the spatial resolution, S/N ratio, and so on, but the throughput of photon might be reduced because the spatial coherence of the entangled photon is not as high as that of laser light. In conclusion, we anticipate that quantum polarization microscopy, utilizing a quantum-entangled photon source, will soon advance toward practical applications in biological imaging and sensing beyond the classical limit, if further improvements such as a reduction in noise and measurement time can be achieved.

Author Contributions: Conceptualization, Y.H.; methodology, Y.H. and M.S. (Mousume Samad); software, M.S. (Mousume Samad); validation, Y.H. and M.S. (Mousume Samad); formal analysis, M.S. (Mousume Samad); investigation, M.S. (Mousume Samad); resources, Y.H.; data curation, M.S. (Mousume Samad); writing—original draft preparation, M.S. (Mousume Samad); writing—review and editing, M.S. (Mousume Samad), Y.H., M.S. (Maki Shimizu); supervision, Y.H. All authors have read and agreed to the published version of the manuscript.

Funding: Part of this study was supported by the JSPS KAKENHI (Grant No. 22K18292 and 23K22787) and JST A-STEP (Grant No. JPMJTR22RD).

Data Availability Statement: The data that support the finding of this study are available from the corresponding author upon reasonable request.

Conflicts of Interest: The authors declare no conflict of interest.

References

1. Gilaberte, B.M.; Setzpfandt, F.; Steinlechner, F.; Beckert, E.; Pertsch, T.; Gräfe, M. Perspectives for applications of quantum imaging. *Laser Photonics Rev.* **2019**, *13*, 1900097. [CrossRef]
2. Morris, P.A.; Aspden, R.S.; Bell, J.E.; Boyd, R.W.; Padgett, M.J. Imaging with a small number of photons. *Nat. Commun.* **2015**, *6*, 5913. [CrossRef] [PubMed]
3. Tenne, R.; Rossman, U.; Rephael, B.; Israel, Y.; Krupinski-Ptaszek, A.; Lapkiewicz, R.; Oron, D. Super-resolution enhancement by quantum image scanning microscopy. *Nat. Photonics* **2019**, *13*, 116–122. [CrossRef]
4. Kviatkovsky, I.; Chrzanowski, H.M.; Avery, E.G.; Bartolomaeus, H.; Ramelow, S. Microscopy with undetected photons in the mid-infrared. *Sci. Adv.* **2020**, *6*, eabd0264. [CrossRef]
5. Defienne, H.; Ndagano, B.; Lyons, A.; Faccio, D. Polarization entanglement-enabled quantum holography. *Nat. Phys.* **2021**, *17*, 591–597. [CrossRef]
6. Casacio, C.A.; Madsen, L.S.; Terrasson, A.; Waleed, M.; Barnscheidt, K.; Hage, B.; Bowen, W.P. Quantum-enhanced nonlinear microscopy. *Nature* **2021**, *594*, 201–206. [CrossRef]
7. Moreau, P.A.; Toninelli, E.; Gregory, T.; Padgett, M.J. Imaging with quantum states of light. *Nat. Rev. Phys.* **2019**, *1*, 367–380. [CrossRef]
8. Shih, Y. Entangled biphoton source-property and preparation. *Rep. Prog. Phys.* **2003**, *66*, 1009. [CrossRef]
9. Horodecki, R.; Horodecki, P.; Horodecki, M.; Horodecki, K. Quantum entanglement. *Rev. Mod. Phys.* **2009**, *81*, 865–942. [CrossRef]
10. Boyd, R.D. *Nonlinear Optics*, 3rd ed.; Elsevier Science: Oxford, UK, 2008; pp. 1–59.
11. Couteau, C. Spontaneous parametric down-conversion. *Contemp. Phys.* **2018**, *59*, 291–304. [CrossRef]
12. Rubin, M.H.; Shih, Y. Resolution of ghost imaging for nondegenerate spontaneous parametric down-conversion. *Phys. Rev. A—At. Mol. Opt. Phy.* **2008**, *78*, 033836. [CrossRef]
13. Karmakar, S.; Shih, Y. Two-color ghost imaging with enhanced angular resolving power. *Phys. Rev. A—At. Mol. Opt. Phys.* **2010**, *81*, 033845. [CrossRef]
14. Lemos, G.B.; Borish, V.; Cole, G.D.; Ramelow, S.; Lapkiewicz, R.; Zeilinger, A. Quantum imaging with undetected photons. *Nature* **2014**, *512*, 409–412. [CrossRef]
15. Kalashnikov, D.A.; Paterova, A.V.; Kulik, S.P.; Krivitsky, L.A. Infrared spectroscopy with visible light. *Nat. Photonics* **2016**, *10*, 98–101. [CrossRef]
16. Kwiat, P.G.; Mattle, K.; Weinfurter, H.; Zeilinger, A.; Sergienko, A.V.; Shih, Y. New high-intensity source of polarization-entangled photon pairs. *Phys. Rev. Lett.* **1995**, *75*, 4337. [CrossRef]
17. Ono, T.; Okamoto, R.; Takeuchi, S. An entanglement-enhanced microscope. *Nat. Commun.* **2013**, *4*, 2426. [CrossRef]
18. Nagata, T.; Okamoto, R.; O'brien, J.L.; Sasaki, K.; Takeuchi, S. Beating the standard quantum limit with four-entangled photons. *Science* **2007**, *316*, 726–729. [CrossRef]
19. Giovannetti, V.; Lloyd, S.; Maccone, L. Quantum metrology. *Phys. Rev. Lett.* **2006**, *96*, 010401. [CrossRef]
20. Zhang, Y.; He, Z.; Tong, X.; Garrett, D.C.; Cao, R.; Wang, L.V. Quantum imaging of biological organisms through spatial and polarization entanglement. *Sci. Adv.* **2024**, *10*, 1495. [CrossRef]
21. He, Z.; Zhang, Y.; Tong, X.; Li, L.; Wang, L.V. Quantum microscopy of cells at the Heisenberg limit. *Nat. Commun.* **2023**, *14*, 2441. [CrossRef]
22. Correlated Photon-Pair Source. Available online: https://www.thorlabs.com/newgrouppage9.cfm?objectgroup_id=13675 (accessed on 29 July 2024).
23. David, S.; Gregg, J. *Quantum Metrology, Imaging, and Communication*; Springer: Berlin/Heidelberg, Germany, 2018. [CrossRef]
24. EDU-QOP1(/M) Quantum Optics Kit. Available online: https://www.thorlabs.com/thorproduct.cfm?partnumber=EDU-QOP1/M (accessed on 9 April 2024).
25. Brida, G.; Chekhova, M.V.; Fornaro, G.A.; Genovese, M.; Lopaeva, E.D.; Berchera, I.R. Systematic analysis of signal-to-noise ratio in bipartite ghost imaging with classical and quantum light. *Phys. Rev. A* **2011**, *83*, 063807. [CrossRef]